Enhanced photocatalytic degradation of organic pollutants and hydrogen production by a visible light–responsive $Bi_2WO_6/ZnIn_2S_4$ heterojunction

Auttaphon Chachvalvutikul[a], Tawanwit Luangwanta[a], Samuel Pattisson[b], Graham J. Hutchings[b], Sulawan Kaowphong[a,c,d,*]

[a] Department of Chemistry, Faculty of Science, Chiang Mai University, Chiang Mai 50200, Thailand

[b] Cardiff Catalysis Institute, School of Chemistry, Cardiff University, Main Building, Park Place CF10 3AT, Cardiff, UK

[c] Center of Excellence in Materials Science and Technology, Chiang Mai University, Chiang Mai 50200, Thailand

[d] Center of Excellence for Innovation in Chemistry, Faculty of Science, Chiang Mai University, Chiang Mai 50200, Thailand

*Corresponding author

E–mail address: sulawank@gmail.com, sulawan.k@cmu.ac.th

Tel: +66 53 943341 Fax: +66 53 892277

Abstract

In this work, we have reported the photocatalytic applications of the direct Z-scheme $Bi_2WO_6/ZnIn_2S_4$ heterojunction in the degradation of organic pollutants and the production of H_2 gas. The nano-spherical shape of Bi_2WO_6 and porous structure of $ZnIn_2S_4$ particles, synthesized using cyclic microwave radiation method, facilitated the intimate interfacial contact of the heterojunction. Consequently, the photocatalytic activity of $Bi_2WO_6/ZnIn_2S_4$ towards degradation of salicylic acid (SA) and methylene blue (MB), the models of non-dye and dye organic pollutants, were maximized after introducing only 12.5%wt of Bi_2WO_6. Similarly, this photocatalyst demonstrated an enhancement in H_2 production in comparison to the single-component photocatalysts. Furthermore, this photocatalyst maintained a high photoactivity after three repeated cycles for MB degradation and H_2 production. The enhanced photo-efficacy of this heterojunction originates from the improved separation and transportation of photogenerated e^-/h^+ through a direct Z-scheme system. This was evidenced by electrochemical analyses and active species trapping experiments, combined with the consideration of reduction potential of reactive oxygen species.

Keywords: $Bi_2WO_6/ZnIn_2S_4$; direct Z-scheme; heterojunction; photodegradation; H_2 production

1. Introduction

Heterogeneous photocatalysis is an alternative technology to overcome the energy crisis and environmental pollution problems [1,2]. Many semiconductor photocatalysts with visible light response have been studied and developed aiming to effectively harness solar energy [3–6]. Ternary metal sulfides have been extensively regarded as visible-light active photocatalysts owing to their relatively narrow band gaps when compared with the relevant

oxide-based photocatalysts [7,8]. Among the ternary metal sulfides, $ZnIn_2S_4$ – the only semiconducting material with a layered structure in the AB_2X_4 family [9] – is a promising candidate as a photocatalyst for various organic transformations [6,10], degradation of organic compounds [11,12] and water splitting for H_2 evolution [13,14]. Unfortunately, a fast recombination rate of e^-/h^+ pairs and photocorrosion restrict its photocatalytic efficiency and therefore further practical applications [15,16].

Forming a heterojunction from two or more materials with compatible band alignments is considered as a facile strategy to decrease the e^-/h^+ recombination rate and enhance the e^-/h^+ pair separation between their individual constituent materials, which results in enhanced photocatalytic efficiency [17]. As reported [18–21], fabrication of the bismuth-based $ZnIn_2S_4$ heterojunctions by combining $ZnIn_2S_4$ with the optimum amounts of bismuth-related materials such as Bi_2S_3, $BiVO_4$, Bi_2MoO_6 and BiOCl can considerably improve the photo-efficacy in comparison to the single materials. Bi_2WO_6 is also one of the attractive bismuth-related photocatalysts due to its the high oxidation ability, enabling a considerable efficiency in the photodegradation of organic compounds [22,23]. As a consequence of these properties and the compatibility of band potentials between Bi_2WO_6 and $ZnIn_2S_4$ [5,20,24], Bi_2WO_6 is considered as a good co-catalyst to combine with $ZnIn_2S_4$. Wan-Kuen Jo *et al*. [24] reported the fabrication of $Bi_2WO_6/ZnIn_2S_4$ composites with different amounts of $ZnIn_2S_4$ in an effort to improve the photoactivity of $ZnIn_2S_4$ for the degradation of pharmaceuticals (metronidazole). Nevertheless, the efficacy of this composite is still poorer than that of $ZnIn_2S_4$. Furthermore, the other photocatalytic applications, particularly the elimination of organic reagents in wastewater and production of H_2 from water splitting were not studied.

In terms of the synthesis of Bi_2WO_6 and $ZnIn_2S_4$ powders, many studies have reported the use of a hydrothermal method [4,10,24–26]. However, a major limitation of this approach is the high energy consumption and requirement of long reaction times. Microwave irradiation

synthesis – an internal heating method – is an alternative approach for the rapid and economical preparation of several semiconductor materials [18,27]. During microwave heating, heat is generated by the interactions between the electromagnetic radiation and dielectric species in a solution medium. By applying the electromagnetic radiation to the reaction system, these species can orientate with the rapidly alternating electric field by rotation, friction and collision. These phenomena lead to an increase in local temperature, enabling short reaction times and high reaction rates. As a result, thermal gradients can be substantially reduced to obtain an efficient and uniform chemical reaction, and thus the desired materials with narrow size-distributed particles can be formed in a relative short time when compared to the external heating methods [27,28].

In this research study, the direct Z-scheme $Bi_2WO_6/ZnIn_2S_4$ heterojunction was applied for degradation of organic pollutants and the production of H_2 gas. Salicylic acid and methylene blue were used as models of non-dye and dye organic pollutants. A cyclic microwave irradiation combined with a wet impregnation method was employed to fabricate $Bi_2WO_6/ZnIn_2S_4$ nanocomposites with different weight percentages of Bi_2WO_6. The photoactivities of these nanocomposites were investigated in comparison with $ZnIn_2S_4$ and Bi_2WO_6. Electrochemical impedance spectroscopy and transient current response measurements were carried out to further examine a charge transfer efficiency and separation of e^-/h^+ pairs. The charge transfer mechanisms for the enhanced photo-efficiency of the $Bi_2WO_6/ZnIn_2S_4$ photocatalyst in all photocatalytic reactions were proposed based on energy band potentials determined from the Mott-Schottky plot combined with the trapping experimental results and the consideration of the reduction potentials of active oxygen species.

2. Experimental Procedure

2.1. Preparation of $ZnIn_2S_4$, Bi_2WO_6 and $Bi_2WO_6/ZnIn_2S_4$ powders

$ZnIn_2S_4$ powder was prepared by dissolving $Zn(NO_3)_2 \cdot 6H_2O$, $InCl_3 \cdot 4H_2O$ and thioacetamide with 1:2:4 mole ratios in ethylene glycol (40.0 mL). The mixture was then placed in the microwave oven (2450 MHz-EMS28205, Electrolux, China) and treated with the microwave radiation at 300 W for different processing cycles (30, 45 and 60 cycles), where one cycle was 30 sec on and 60 sec off. For the preparation of Bi_2WO_6 powder, $Bi(NO_3)_3 \cdot 5H_2O$ and $Na_2WO_4 \cdot 2H_2O$ with 2:1 mole ratios were mixed in DI water (40.0 mL) under vigorous stirring. The mixture was then treated with the microwave radiation (600 W, 30 cycles). The collected powder was dried and further calcined (500 °C, 5 h).

The $Bi_2WO_6/ZnIn_2S_4$ nanocomposites were fabricated using a procedure similar to that in our previously reported study [18]. The fabricated $Bi_2WO_6/ZnIn_2S_4$ powders were designated as x%wt-$Bi_2WO_6/ZnIn_2S_4$, where x represents 6.25, 10, 12.5, 18 and 25%wt of Bi_2WO_6. A physical mixture sample, designated as PM, was also prepared by a physical grinding of the Bi_2WO_6 and $ZnIn_2S_4$ powders together for comparison.

2.2. Characterizations

X-ray diffraction (XRD) spectra of the synthesized powders were recorded by a Rigaku Smartlab X-ray diffractometer to determine their purity and structure. The JEOL JSM-6335F and JEOL JEM-2010 electron microscopes were used to record the field emission scanning electron microscopic (FESEM) and transmission electron microscopic (TEM) images of the samples. Energy-dispersive X-ray spectroscopy (EDS) and X-ray photoelectron spectroscopy (XPS, AXIS Ultra DLD, Kratos Analytical Ltd.) were used to analyze elemental compositions in the samples. Electron paramagnetic resonance (EPR) spectrum was recorded on a Bruker EMX-Micro spectrometer at room temperature with a modulation frequency of 100.00 kHz.

Optical properties were studied by a UV-visible diffuse reflectance spectrophotometer (UV-vis DRS, UV-1800 Shimadzu) with barium sulfate ($BaSO_4$) as a reference material, and an Avantes AvaSpec-2048TEC-USB2 photoluminescence spectrometer. The surface area and porosities of the samples were investigated by N_2 adsorption at -196 ^oC using a NOVA-e, Quantachrome instrument and calculated by the Brunauer-Emmett-Teller (BET) and Barrett-Joyner-Halenda (BJH) methods, respectively. Prior the analysis, the samples were degassed at 200 ^oC for 3 h under vacuum.

Electrochemical impedance spectroscopy (EIS), transient photocurrent response and Mott-Schottky measurements were performed on a PGSTAT128N Autolab Potentiostat/galvanostat instrument (Metrohm Siam Ltd.) with a sample deposited on a FTO coated glass substrate as a working electrode, Pt wire as a counter electrode, Ag/AgCl (3 M KCl) as a reference electrode, and Na_2SO_4 solution (0.1 M, pH ~6) as an electrolyte. The EIS spectra were recorded by employing a bias potential of 1.5 V with a frequency in the range of 0.01 Hz to 10^5 Hz and an amplitude of 0.05 V without light irradiation. The transient photocurrent response was measured in a light on–off process with a pulse of 30 s and an applied potential of 1.0 V. A 50 W LED lamp was used as a visible-light source (Model COB LED CHIP, YNL [29]). The Mott-Schottky plots were analyzed at 10 Hz frequency and 5 mV amplitude.

2.3. Photocatalytic degradation and H_2 production tests

The photocatalyst (50 mg) was dispersed in an aqueous solution containing an organic substrate (100 mL of methylene blue (MB) or salicylic acid (SA)). The concentrations of MB and SA solutions were 1.25×10^{-4} and 2.0×10^{-5} mol L^{-1}, respectively. The suspension was stirred for 30 min in the dark, followed by irradiation under the 50 W LED light (Model COB LED CHIP, YNL [29]) for 300 min. Every 60 min of the reaction, the solution (2 mL) was

taken. The concentrations of the residual organic compounds at different reaction times were monitored by the UV-1800 Shimadzu spectrophotometer at the wavelength of maximum absorbance. The photodegradation efficiency (%DE) and reaction kinetics were calculated using the following equations:

$$\%DE = \frac{A_0 - A}{A_0} x100 \quad (1)$$

$$\ln\left(\frac{A_0}{A}\right) = kt \quad (2)$$

where A_0 and A represent the initial and the remaining concentrations of MB (or SA) solution, respectively. The k and t represent the initial rate constant and reaction time, respectively. A blank experiment without the addition of the photocatalyst (photolysis) was also conducted under the same experimental conditions to make sure that the degradation of organic compounds certainly takes place due to the photocatalytic reaction. Total organic carbon (TOC) of the supernatant solution after 300 min of irradiation was determined on a TOC analyzer (Multi N/C 3100, Analytik Jena AG). Trapping experiments were performed in the reaction solution containing SA and 12.5%wt-Bi_2WO_6/$ZnIn_2S_4$ photocatalyst. Various reagents (1 mmol L^{-1}) were used as scavengers, such as ascorbic acid (ASC) [30], isopropyl alcohol (iPrOH) [31], ethylenediaminetetraacetic acid disodium salt (EDTA-2Na) [30], potassium persulfate ($K_2S_2O_8$) [32], were added into the reaction solution to trap superoxide radicals ($O_2^{\bullet-}$), hydroxyl radicals ($^{\bullet}OH$), holes (h^+) and electrons (e^-), respectively.

The nitrotetrazolium blue transformation (NBT) method was used to confirm the detection of $O_2^{\bullet-}$ radicals generated during the photocatalytic reaction [33]. The test procedures were as follows: the photocatalyst (50 mg) was dispersed in 100 mL of the NBT solution ($2.0x10^{-5}$ mol L^{-1}) and then the suspension was irradiated under 50 W LED light for 60 min. Finally, the suspension was centrifuged, and the absorption spectrum of the supernatant solution was measured using UV-vis spectrophotometer at 265 nm. The $^{\bullet}OH$ radicals can be detected by benzoic acid hydroxylation method [34]. Firstly, the photocatalyst (50 mg) was

dispersed in 100 mL of the benzoic acid solution ($2.0x10^{-5}$ mol L^{-1}) and then the suspension was irradiated under 50 W LED light for 60 min, yields *o*-hydroxybenzoic acid. Following this, an $FeCl_3$ solution was dropped into the supernatant solution to form a Fe(III)-hydroxybenzoic acid complex. Finally, the complex solution was measured at a wavelength of 520 nm by UV-vis spectrophotometer.

For the photocatalytic H_2 production test, the photocatalyst (20 mg) was dispersed in an aqueous solution containing methanol (20%v/v). The suspension was stirred in the dark under argon gas flowing for 30 min and then exposed to the 150 W xenon light (Model 6256, Newport [29]) for 180 min. The produced gas (5 mL) was sampled at every 30 min of irradiation and the concentrations of H_2 gas were then analyzed using a PerkinElmer Clarus 480 gas chromatograph.

Reusability and stability of the photocatalyst for the MB degradation and H_2 evolution reactions were examined. After the first run of the reaction, the photocatalyst was recovered from the reaction solution by centrifugation. The recovered photocatalyst sample was then washed with DI water for several times and dried. Three cycles of the photocatalytic reactions were performed under the same conditions. The reused photocatalyst was further characterized by XRD and FESEM.

3. Results and Discussion

3.1. Photocatalytic activity of the $ZnIn_2S_4$ samples synthesized at different microwave irradiation cycles

The XRD spectra of the synthesized $ZnIn_2S_4$ powders are shown in Error! Reference source not found.**(a)**. All of the spectra show diffraction peaks of (006), (101), (102), (103), (104), and (110) planes at 2θ of 21.59°, 26.95°, 27.69°, 28.51°, 30.20° and 47.18°, respectively,

corresponding to the XRD pattern of a hexagonal $ZnIn_2S_4$ structure (JCPDS No. 01-072-0773). No possible impurities are observed. The peak broadening implies that the crystallite size is in the nanoscale. Their FESEM images are shown in **Error! Reference source not found.(b)-(d)**. At 30 cycles, incomplete flower-like microspheres are formed. The powder is composed of mainly aggregated particles and partially collapsed nanosheets. More complete flower-like microspheres are observed after being irradiated for 45 cycles and the perfect flower-like microspheres can be obtained at 60 cycles. The diameter of the flower-like $ZnIn_2S_4$ microspheres increased with prolonged processing times (0.32, 0.38 μm and 0.53 μm for the 30, 45 and 60 cycles, respectively). The microstructures of these $ZnIn_2S_4$ powders shown in the TEM images (Error! Reference source not found.**(e)-(g)**) appear to be the flower-like microspheres that are built up of thin nanosheets with the average thicknesses of 106, 13 and 9 nm for the powders synthesized using 30, 45 and 60 cycles, respectively. These results imply that processing cycles affect the morphology, microstructure and size of the synthesized $ZnIn_2S_4$ particles. The SAED patterns (**Fig. S1**) of all $ZnIn_2S_4$ powders were indexed to the (102), (104) and (110) planes of hexagonal $ZnIn_2S_4$ crystalline structure, according to the JCPDS database.

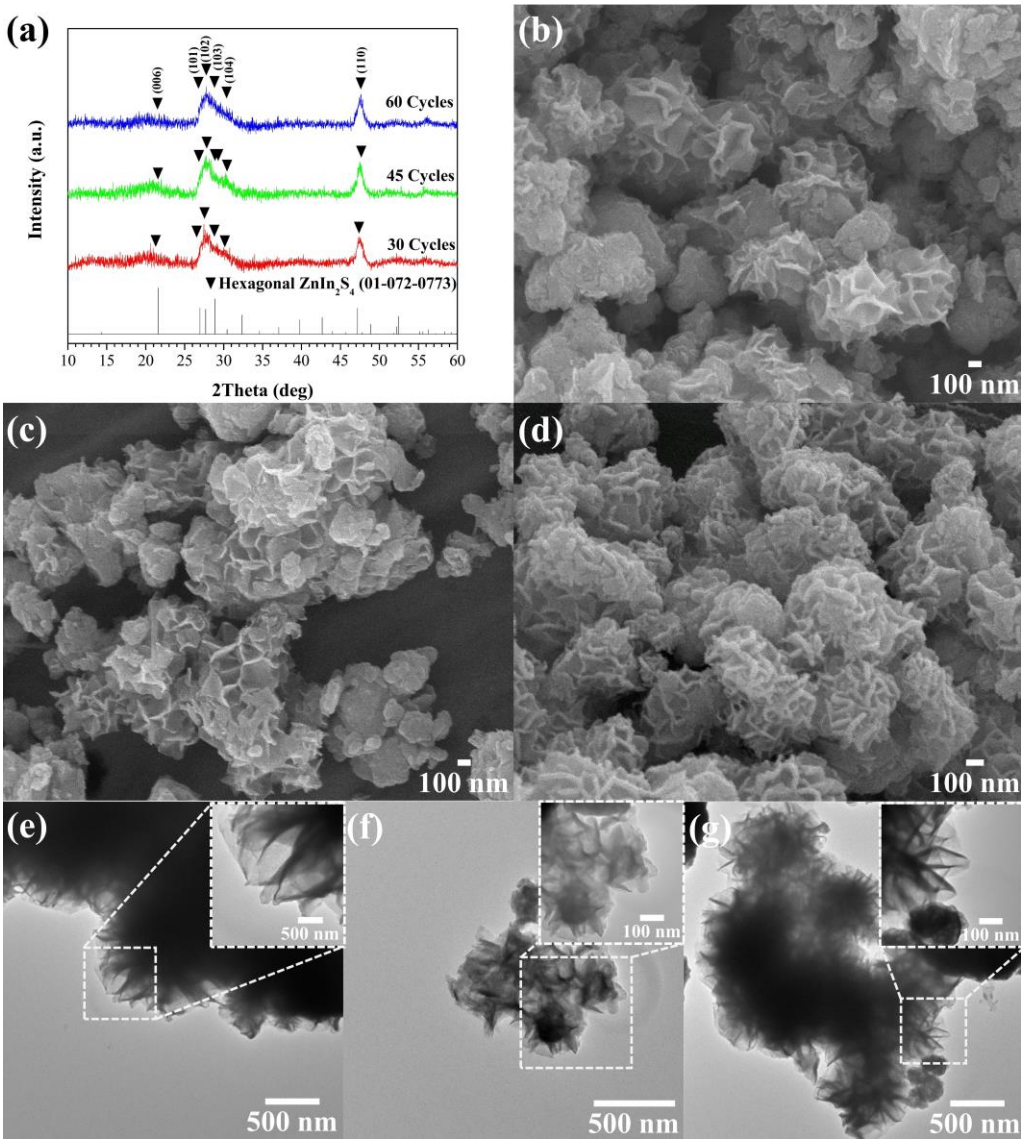

Fig. 1. (a) XRD spectra of the $ZnIn_2S_4$ samples. **(b-d)** FESEM and **(e-g)** TEM images of the $ZnIn_2S_4$ samples synthesized using 30, 45 and 60 cycles, respectively. Insets of **(e)-(g)**: the high-magnification TEM images.

The UV-vis DRS spectra of the $ZnIn_2S_4$ samples (**Fig. 2(a)**) appear in the visible light region. Regarding the direct transition of $ZnIn_2S_4$ [18], the band gap energy (E_g) values, estimated from the Tauc's plots, were 2.42, 2.43, and 2.45 eV for the $ZnIn_2S_4$ powders synthesized at 30, 45 and 60 cycles, respectively. There is no significant difference in the absorption edges and E_g values of these samples, suggesting the minor role of the light

absorption properties in their photocatalytic activity. However, visible-light absorption ability of the $ZnIn_2S_4$ synthesized at 60 cycles is better than those of the others, implying that this sample can effectively utilize visible light, and thus e^-/h^+ pairs can be produced more efficiently. EDS and XPS analyses can be used to determine the bulk and surface elemental compositions of materials, respectively [35]. The elemental compositions obtained from the EDS and XPS analyses of $ZnIn_2S_4$ synthesized at 60 cycles reveal the atomic ratios of Zn, In, and S elements of 1 : 2.21 : 3.47 (**Fig. S2(a)**) and 1 : 2.49 : 3.54 (**Fig. S2(b)**), respectively. These elemental analyses suggest that sulfur vacancies could exist in the synthesized $ZnIn_2S_4$ material. EPR measurement of $ZnIn_2S_4$ was carried out to further confirm the existence of sulfur vacancies on the surface of $ZnIn_2S_4$. The $ZnIn_2S_4$ shows a strong EPR signal at g = 2.003 (**Fig. S2(c)**) which indicates an entrapment of electrons in sulfur vacancies [36–38]. These results infer that sulfur vacancies are generated not only on the surface of $ZnIn_2S_4$ but also throughout the bulk $ZnIn_2S_4$ porous structure. The formation of sulfur vacancies in the $ZnIn_2S_4$ structure is probably attributed to the decrease in the barrier of nucleation and ultrafast crystallization of $ZnIn_2S_4$ induced by microwave irradiation [39].

Photodegradation efficiency of all $ZnIn_2S_4$ samples for the MB degradation are shown in **Fig. 2(b)** and **Fig. S3.** Among the other $ZnIn_2S_4$ photocatalysts, the $ZnIn_2S_4$ photocatalyst synthesized using 60 cycles exhibits the highest efficiency (%DE = 59.8% and *k* values = 0.0033 min^{-1}), which could be attributed to the perfect, flower-like, microstructure of this photocatalyst. This hierarchical three-dimensional structure facilitates the efficient light harvesting and multi–reflections of the incident light within its structure, as evidenced by its visible light absorption ability (**Fig. 2(a)**). Moreover, the BET analysis reveal that the surface area values of the $ZnIn_2S_4$ powders synthesized at 30, 45, and 60 cycles are 77.0, 86.7, and 102.1 m^2g^{-1} with the total pore volume values of 0.2484, 0.2874 and 0.3434 cm^3g^{-1}, respectively. The N_2 adsorption-desorption isotherms and the corresponding curves of the pore

size distribution are provided in **Fig. 2(c)** and **(d)**, respectively. All $ZnIn_2S_4$ samples exhibit type-IV isotherms with recognizable H3 type hysteresis loops in the range of 0.4-1.0 P/P_0. The shape of the hysteresis loop associated with slit-like mesopores formed by the aggregations of plate-like particles [40,41] that are produced by microwave irradiation route. In addition, the pore size distribution curves confirm that the $ZnIn_2S_4$ samples have mesopores with pore diameters in the range of 15-20 nm and the pore volume of the $ZnIn_2S_4$ synthesized at 60 cycles is the highest. The larger surface area and greater total pore volume of the $ZnIn_2S_4$ synthesized at 60 cycles result in more available sites for the organic molecules to adsorb on its porous structure, which are favourable to the photocatalytic reaction between the adsorbed organic molecules and the charge carriers that are migrated to the surface photocatalyst during the photocatalysis.

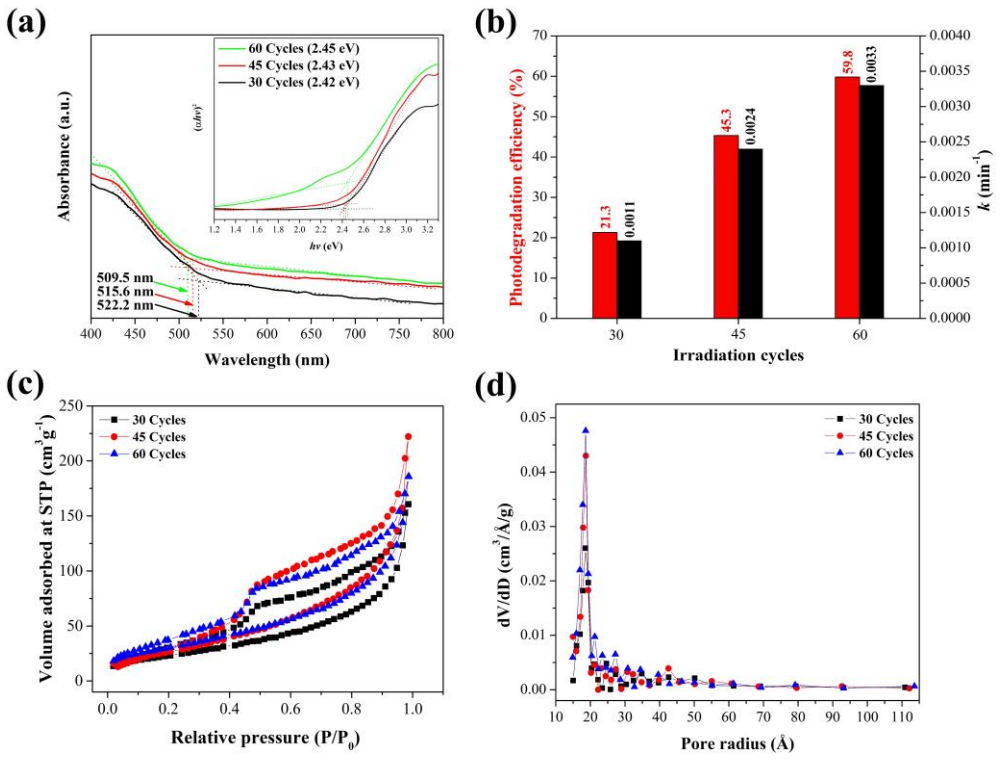

Fig. 2. (a) UV-vis DRS spectra with the Tauc's plots (inset of (a)) of the $ZnIn_2S_4$ samples. **(b)** Photocatalytic degradation of MB by the $ZnIn_2S_4$ samples. **(c)** The N_2 adsorption-desorption isotherms and **(d)** the corresponding pore size distribution curves of all $ZnIn_2S_4$ samples.

3.2. Photocatalytic activities of the $Bi_2WO_6/ZnIn_2S_4$ nanocomposites

3.2.1. Characterizations of the photocatalyst samples

Fig. 3 shows XRD spectra of the $Bi_2WO_6/ZnIn_2S_4$ nanocomposite powders in comparison with pure Bi_2WO_6 and $ZnIn_2S_4$. The XRD spectrum of Bi_2WO_6 reveals the main signals at 28.30°, 32.67°, 47.14°, 55.82° and 58.54°, which are, respectively, indexed as (131), (060), (202), (331) and (262) crystal planes of an orthorhombic Bi_2WO_6 structure (JCPDS No. 00-039-0256). No possible impurities are observed, suggesting its high purity. For the $Bi_2WO_6/ZnIn_2S_4$ nanocomposites, the major characteristic diffraction peaks of hexagonal $ZnIn_2S_4$ and orthorhombic Bi_2WO_6 phases are observed, indicating that $ZnIn_2S_4$ and Bi_2WO_6 coexist in the nanocomposites. In addition, with increasing weight percentages of Bi_2WO_6 in the $Bi_2WO_6/ZnIn_2S_4$ nanocomposites, the diffraction peaks of Bi_2WO_6 gradually strengthen in the intensity while the diffraction peak intensities of $ZnIn_2S_4$ gradually decrease. Moreover, the XRD peak positions for the nanocomposites do not shift compared with those of pure Bi_2WO_6 and $ZnIn_2S_4$, implying that the crystal structures of these compounds are not destroyed after being fabricated by the wet-impregnation method.

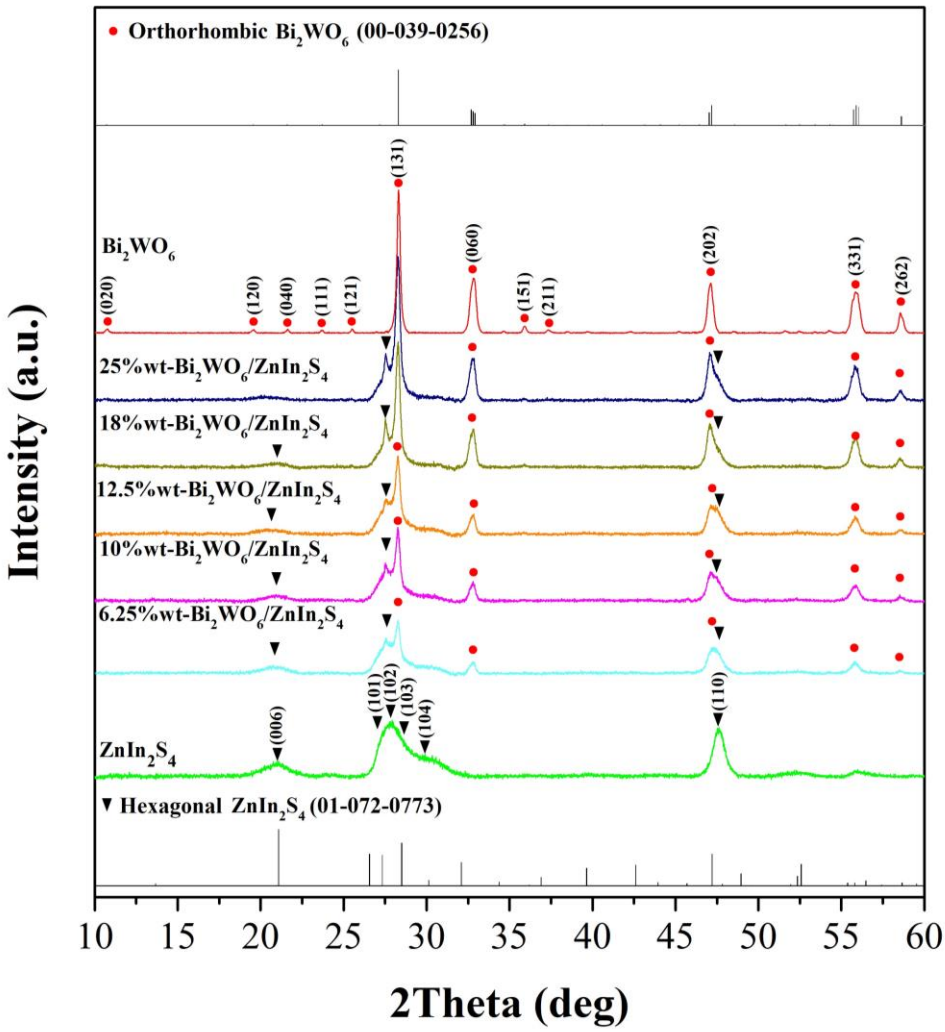

Fig. 3. XRD spectra of the $ZnIn_2S_4$, Bi_2WO_6 and $Bi_2WO_6/ZnIn_2S_4$ powders.

FESEM (**Fig. 4(c)**) and TEM images (**Fig. 5(a)**) of the 12.5%wt-$Bi_2WO_6/ZnIn_2S_4$ nanocomposite reveals that the uniform size distribution of spherical Bi_2WO_6 nanoparticles with an estimated diameter of around 50 nm (**Fig. 4(b)**) deposit on the surface of the $ZnIn_2S_4$ microspheres (**Fig. 4(a)**). EDS spectrum (**Fig. 4(d)**) exhibits the X-ray energies of the Zn, In, S, Bi, W and O elements, verifying that this nanocomposite consists of $ZnIn_2S_4$ and Bi_2WO_6. The atomic ratio of Zn, In and S in 12.5%wt-$Bi_2WO_6/ZnIn_2S_4$ is 1 : 2.21 : 2.80. The low content of S element corresponds to the above elemental analyses for $ZnIn_2S_4$. The TEM images at high-magnification of the marked area shown in **Fig. 5(a)** reveal the lattice spacings of 0.320

nm (**Fig. 5(b)** and 0.193 nm (**Fig. 5(c)**) which can be attributed to (102) and (202) planes of hexagonal $ZnIn_2S_4$ and orthorhombic Bi_2WO_6 crystalline structures, respectively. This implies that the nanocomposite is highly crystalline, and the $ZnIn_2S_4$ and Bi_2WO_6 particles in the nanocomposite are coupled with intimate contact. Scanning TEM – EDS elemental mapping images of the nanocomposite sample (**Fig. 5(d)-(i)**) present homogeneous distributions of Zn, In, S, Bi, W and O elements, confirming the successful fabrication of $Bi_2WO_6/ZnIn_2S_4$ heterostructure.

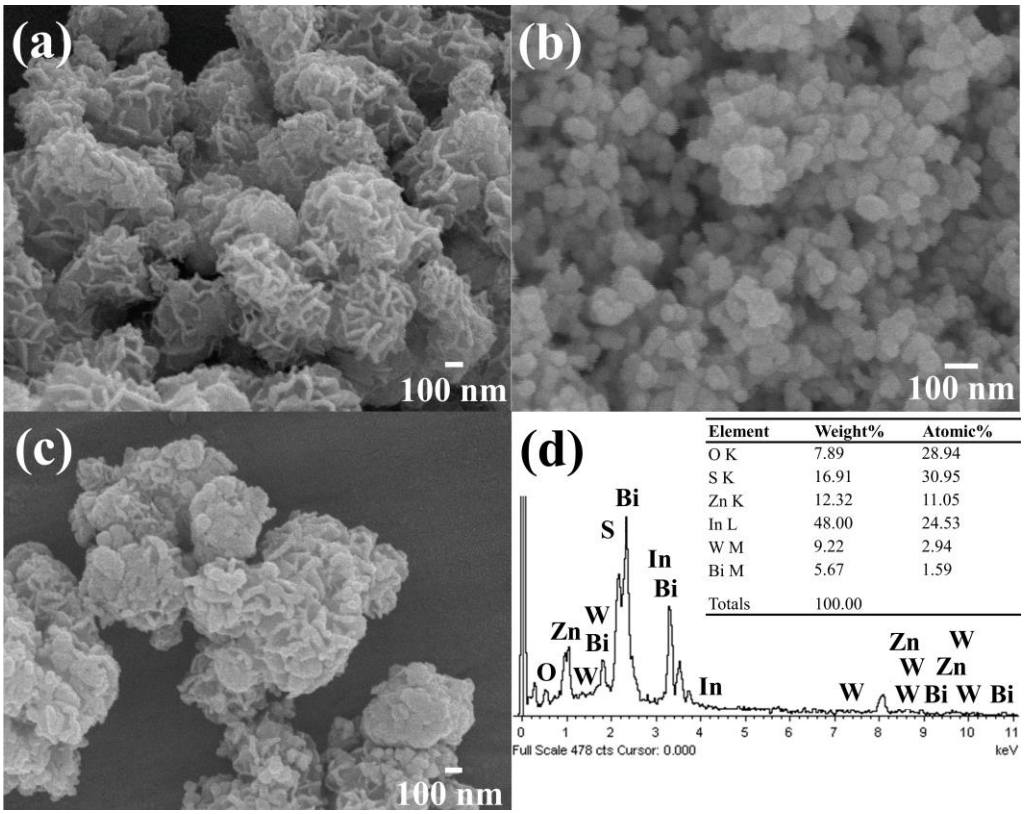

Fig. 4. FESEM images of **(a)** $ZnIn_2S_4$, **(b)** Bi_2WO_6 and **(c)** 12.5%wt-$Bi_2WO_6/ZnIn_2S_4$. **(d)** The EDS spectrum of 12.5%wt-$Bi_2WO_6/ZnIn_2S_4$.

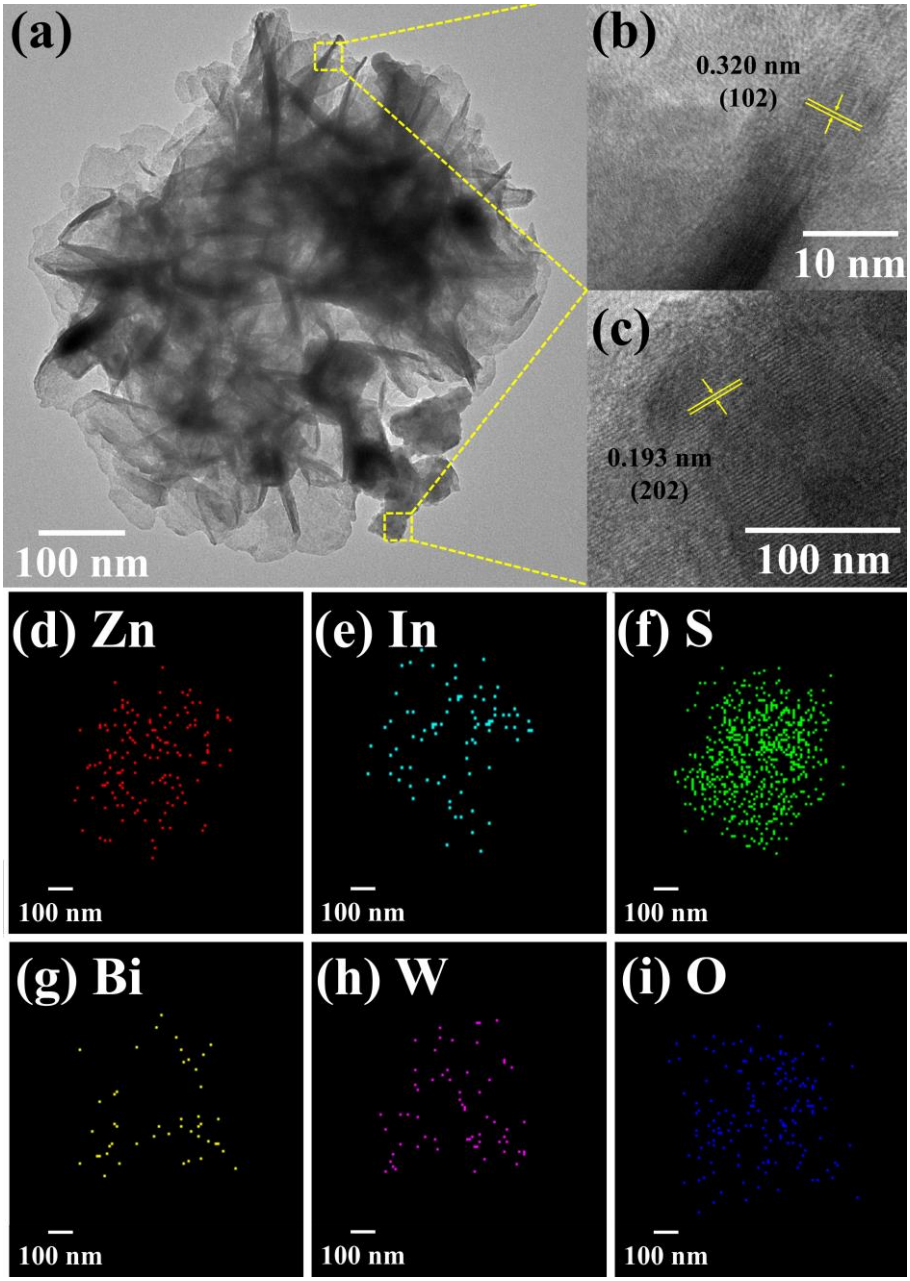

Fig. 5. (a) TEM image of 12.5%wt-$Bi_2WO_6/ZnIn_2S_4$ and **(b)-(c)** TEM images of the marked area at high-magnification shown in Fig. (a). **(d)-(i)** The scanning TEM-EDS elemental mapping images of 12.5%wt-$Bi_2WO_6/ZnIn_2S_4$.

The survey XPS spectrum of 12.5%wt-$Bi_2WO_6/ZnIn_2S_4$ (**Fig. 6(a)**) contains the appearance of XPS signals of Zn, In, S, Bi, W and O elements which is in agreement with the above EDS analysis. The C 1s signal appeared at 284.6 eV is a result from an adventitious carbon or from the carbon that was used for an energy referencing [10]. The spectrum of Zn 2p

for $ZnIn_2S_4$ (**Fig. 6(b)**) exhibits two peaks at 1022.13 and 1045.12 eV, assigning to the binding energies of Zn $2p_{3/2}$ and Zn $2p_{1/2}$ of Zn^{2+} [24]. After combining with Bi_2WO_6, these peaks slightly shift to 1022.03 and 1045.05 eV, respectively. The spectrum of In 3d for $Bi_2WO_6/ZnIn_2S_4$ and $ZnIn_2S_4$ is shown in **Fig. 6(c)**. For $ZnIn_2S_4$, the peaks appeared at 445.20 and 452.82 eV correspond to In $3d_{5/2}$ and In $3d_{3/2}$ of In^{3+}, respectively [24]. For the nanocomposite, the binding energies of In 3d peaks shift to higher values (445.35 and 452.93 eV for In $3d_{5/2}$ and In $3d_{3/2}$, respectively). In **Fig. 6(d)**, the S 2p region for $ZnIn_2S_4$ can be divided into two peaks at 161.94 and 163.17 eV, which are attributed to S $2p_{3/2}$ and S $2p_{1/2}$ of S^{2-} [24], respectively. For the nanocomposite, the S 2p signals positively shift to 162.05 and 163.26 eV, respectively. XPS spectrum of Bi 4f for Bi_2WO_6 (**Fig. 6(e)**) shows two strong peaks at 159.63 and 164.91 eV, attributed to the Bi $4f_{7/2}$ and Bi $4f_{5/2}$ of Bi^{3+}, respectively [26]. After combining with $ZnIn_2S_4$, the Bi 4f signals shift to the lower binding energies (159.47 and 164.69 eV for Bi $4f_{7/2}$ and Bi $4f_{5/2}$, respectively). The XPS spectra of W 4f in Bi_2WO_6 (**Fig. 6(f)**) shows two peaks at 35.93 and 38.05 eV, attributed to the W $4f_{7/2}$ and W $4f_{5/2}$ of W^{6+}, respectively [26]. Introducing Bi_2WO_6 to form the nanocomposite leads to the negatively shift of the W 4f peaks (35.79 eV and 37.86 eV for W $4f_{7/2}$ and W $4f_{5/2}$ peaks, respectively). Besides, the O 1s signals of Bi_2WO_6 and the nanocomposite are observed at 530.54 eV and 532.15 eV, respectively (**Fig. 6(g)**) [26]. The shifts in the binding energy values of the elements in this nanocomposite are the result of the change in outer electron cloud density around these elements after the formation of $Bi_2WO_6/ZnIn_2S_4$ heterojunction. This indicates that a strong interfacial interaction between these two components in the nanocomposite is formed rather than a simple physical interaction [24,42,43], corresponding with the results obtained from the TEM images (**Fig. 5(a)-(c)**). This interaction could allow the transfer of charge carriers during photocatalysis and consequently its photocatalytic activity could be enhanced [44].

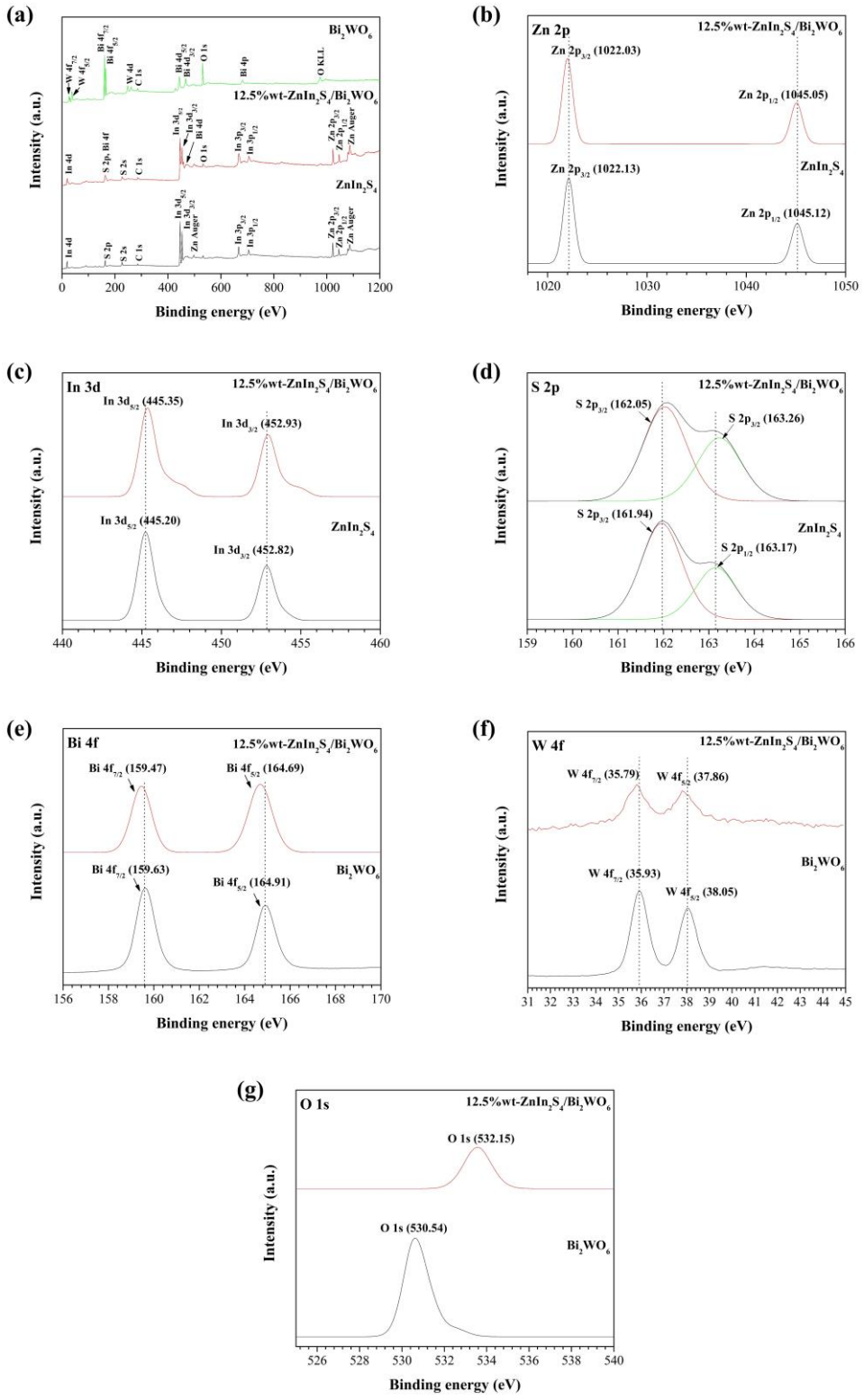

Fig. 6. (a) Survey XPS spectra of Bi_2WO_6, $ZnIn_2S_4$ and 12.5%wt-Bi_2WO_6/$ZnIn_2S_4$. XPS spectra of **(b)** Zn 2p, **(c)** In 3d, **(d)** S 2p, **(e)** Bi 4f, **(f)** W 4f and **(g)** O 1s.

UV-vis DRS spectra of Bi_2WO_6, $ZnIn_2S_4$ and 12.5%wt-Bi_2WO_6/$ZnIn_2S_4$ shown in **Fig. 7(a)** exhibit the absorption of light in the visible-light region, implying their visible-light responsive behavior. The absorption edge of 12.5%wt-Bi_2WO_6/$ZnIn_2S_4$ shifts to a longer wavelength position in comparison with that of Bi_2WO_6, suggesting that Bi_2WO_6 was successfully coupled with $ZnIn_2S_4$. Moreover, the absorption intensity of the nanocomposite is considerably stronger than that of Bi_2WO_6, implying that the nanocomposite can utilize visible light more efficiently and consequently produces a greater number of photogenerated charges during photocatalysis. The E_g value of Bi_2WO_6, determined from the Tauc plots (**Fig. 7(b)**) based on the direct allowed transition in Bi_2WO_6 [25], was 2.82 eV. The PL emission intensity of 12.5%wt-Bi_2WO_6/$ZnIn_2S_4$ nanocomposite shown in **Fig. 7(c)** is lower than those of $ZnIn_2S_4$ and Bi_2WO_6, indicating that the recombination probability of e^-/h^+ pairs in the nanocomposite is efficiently suppressed. An EIS Nyquist plot of the 12.5%wt-Bi_2WO_6/$ZnIn_2S_4$ electrode (**Fig. 7(d)**) exhibits the smallest arc diameter in comparison to that of the pure Bi_2WO_6 and $ZnIn_2S_4$ electrodes, implying the lowest electron transfer resistance on the electrode's surface [15]. Moreover, the transient photocurrent response (**Fig. S4**) shows that the 12.5%wt-Bi_2WO_6/$ZnIn_2S_4$ electrode provides photocurrent density of 0.52 μAcm^{-2} which is about 2.4 and 18 times higher than those of $ZnIn_2S_4$ (0.22 μAcm^{-2}) and Bi_2WO_6 (0.029 μAcm^{-2}), respectively. These outcomes result from the effective e^-/h^+ separation and transportation at the Bi_2WO_6/$ZnIn_2S_4$ heterojunction interface [43,45–47]. The positive slope in the Mott-Schottky plots of both Bi_2WO_6 (**Fig. 7(e)**) and $ZnIn_2S_4$ (**Fig. 7(f)**) indicates their n-type character. The flat-band potentials (E_{fb}), determined from the x-intercept of the curves, are -0.40 and -0.81 V for Bi_2WO_6 and $ZnIn_2S_4$, respectively. The potentials in NHE scale (E_{NHE}) were calculated by the following equation:

$$E_{NHE} = E_{Ag/AgCl} + 0.21 \qquad (3)$$

Consequently, the E_{fb} values of Bi_2WO_6 and $ZnIn_2S_4$ are -0.19 and -0.60 V (*vs.* NHE), respectively. For the n-type semiconductor, a conduction band potential (E_{CB}) is about 0.1 eV above its E_{fb} level [48]. Thus, E_{CB} of Bi_2WO_6 and $ZnIn_2S_4$ are -0.29 and -0.70 V (*vs.* NHE), respectively. Combining these values with the E_g values, the valence band potentials (E_{VB}) of Bi_2WO_6 and $ZnIn_2S_4$ are 2.53 and 1.75 V (*vs.* NHE), respectively.

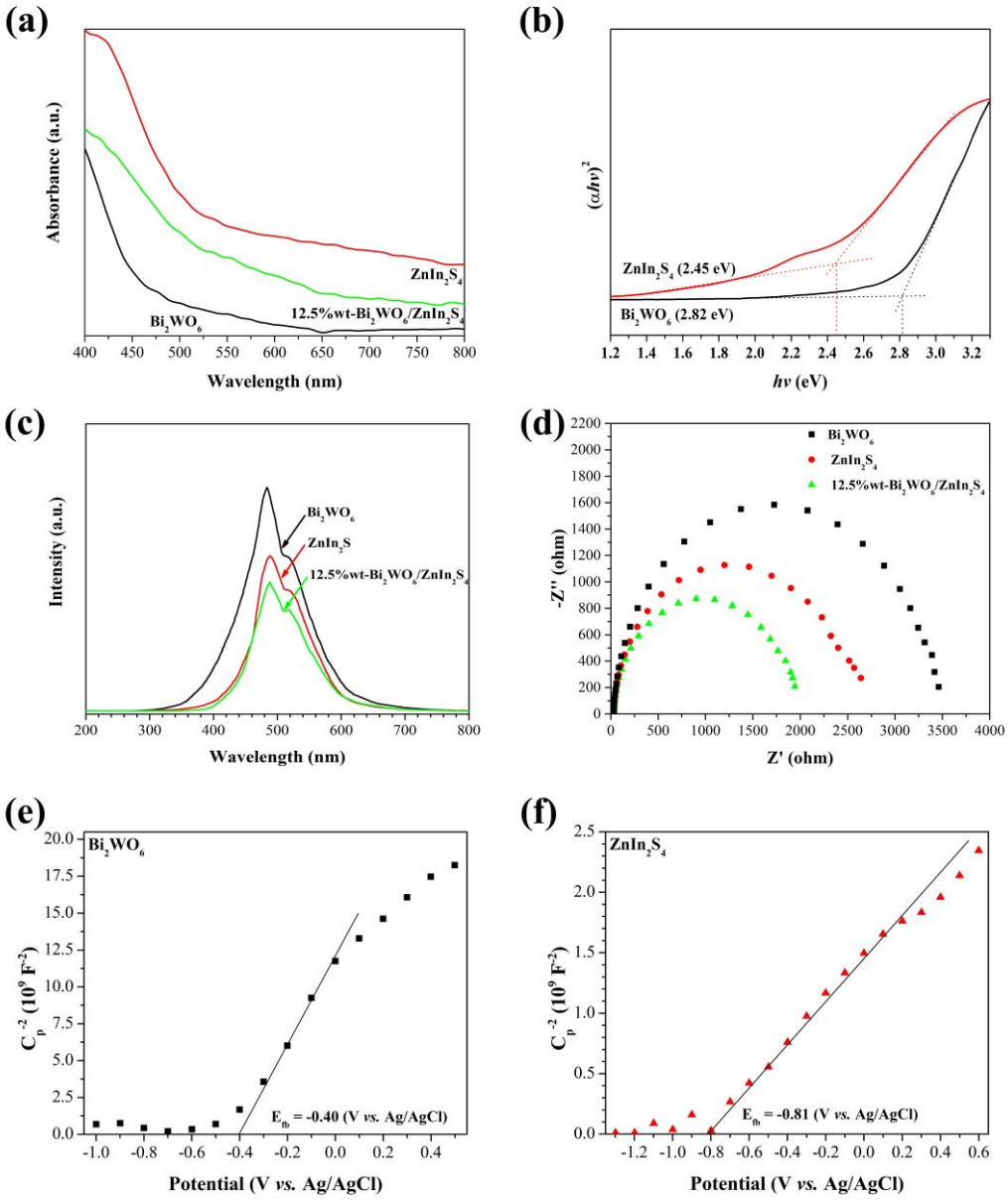

Fig. 7. (a) UV-vis DRS spectra of Bi_2WO_6, $ZnIn_2S_4$ and 12.5%wt-Bi_2WO_6/$ZnIn_2S_4$, and **(b)** Tauc's plots of Bi_2WO_6 and $ZnIn_2S_4$. **(c)** Photoluminescence spectra (λ_{ex} = 345 nm) **(d)** EIS

Nyquist plot of 12.5%wt-$Bi_2WO_6/ZnIn_2S_4$ in comparison to Bi_2WO_6 and $ZnIn_2S_4$. **(e)** and **(f)** Mott-Schottky plots of Bi_2WO_6 and $ZnIn_2S_4$, respectively.

3.2.2. Photocatalytic degradation of organic compounds

Photocatalytic activity results for the degradations of MB and SA are presented in **Fig. 8(a)** and **(b)**, respectively. Without photocatalyst, both MB and SA show no apparent changes in concentration, implying that self-decomposition (photolysis) of these organic compounds under visible light irradiation is negligible. $ZnIn_2S_4$ alone can degrade 59.8% of MB while Bi_2WO_6 barely degrades MB (**Fig. 8(a)**). For the degradation of SA, $ZnIn_2S_4$ and Bi_2WO_6 can degrade 53.2% and 14.0% of SA, respectively. The higher photoactivity of $ZnIn_2S_4$ results from its better light absorption ability and electrochemical properties, as mentioned in the above UV-vis DRS, EIS and transient photocurrent response results.

After formation of $Bi_2WO_6/ZnIn_2S_4$ heterojunctions, photodegradation efficiencies of these photocatalysts towards MB and SA gradually increase with increased amount of Bi_2WO_6 (6.25, 10 and 12.5%wt). A decline in the photodegradation efficiency is observed when the amount of Bi_2WO_6 is further increased to 18%wt and 25%wt. This finding can be attributed to covering and shielding of the active site of the surface of $ZnIn_2S_4$ particles by the excessive quantity of the less-active Bi_2WO_6 nanoparticles as observed in the FESEM images (**Fig. S5**). In addition, a few Bi_2WO_6 (6.25 and 10%wt) nanoparticles distributed on the surface of the $ZnIn_2S_4$ particles (**Fig. S5)** also decrease the efficiency of $Bi_2WO_6/ZnIn_2S_4$. Among the heterojunction photocatalysts, 12.5%wt-$Bi_2WO_6/ZnIn_2S_4$ provides the highest photodegradation efficiency; 95.0% of MB and 72.0% of SA are degraded within 300 min. The initial rate constant (k) for the MB and SA photodegradations were calculated and the results are shown in **Fig. 8(c)** and **(d)**. The k value for the MB degradation over 12.5%wt-$Bi_2WO_6/ZnIn_2S_4$ photocatalyst is 9.8×10^{-3} min^{-1} which is 3.0 times greater than that for

$ZnIn_2S_4$ ($3.3x10^{-3}$ min^{-1}). This nanocomposite photocatalyst can also degrade SA with the highest *k* value ($5.0x10^{-3}$ min^{-1}) among the other photocatalysts. The improvement of the kinetic rate for degradation of SA is 1.7 times higher than that of $ZnIn_2S_4$. The photodegradation efficiencies, calculated *k* values and R^2 of the SA and MB degradation for all photocatalysts are summarized in **Table S1** and the kinetic plots are presented in **Fig. S6**. Herein, the photocatalytic activity of $Bi_2WO_6/ZnIn_2S_4$ is maximized after introducing only 12.5%wt of Bi_2WO_6, which is lower than that stated in the previous report (50%wt of Bi_2WO_6) [24]. This finding could be due to the nano-spherical shape of Bi_2WO_6 and the porous structure of $ZnIn_2S_4$ particles, synthesized using cyclic microwave irradiation method, which greatly facilitates the intimate interfacial contact between these Bi_2WO_6 and $ZnIn_2S_4$ particles. Consequently, charge separation and migration between the two components are efficiently promoted. Notably, the 12.5%wt-$Bi_2WO_6/ZnIn_2S_4$ sample obtained from the physical mixing gives lower photocatalytic activity (%DE = 23.1% and 51.0% for MB and SA, respectively) than that of the 12.5%wt-$Bi_2WO_6/ZnIn_2S_4$ sample obtained from the chemically mixing. This result indicates that the enhanced activity results from the formation of the $Bi_2WO_6/ZnIn_2S_4$ heterojunction that has been fabricated by the synthetic strategy used in this work rather than the simple physical mixing. The recyclability of the 12.5%wt-$Bi_2WO_6/ZnIn_2S_4$ heterojunction towards the MB degradation (**Fig. 8(e)**) shows no notable decrease in the degradation is observed during the three-run test, even though the MB molecules with intense blue color are adsorbed on surface of the photocatalyst which might suppress its light absorption capability. This finding verifies the recyclability and good stability of the 12.5%wt-$Bi_2WO_6/ZnIn_2S_4$ heterojunction for use as the photocatalyst in the photodegradation of organic dyes.

Usually, the photodegradation reactions of organic dyes containing *N*-alkyl groups are parallel and/or competitively proceeded by destruction of the chromophore structure and *N*-de-alkylation processes. The MB degradation mechanism can be monitored by the changes in the

absorption spectra of the MB supernatant solutions during the photodegradation reaction in the presence of the $Bi_2WO_6/ZnIn_2S_4$ photocatalyst as illustrated in **Fig. S7(a)**. As can be seen, the characteristic absorption band of MB decreases with a concomitant wavelength shift to shorter wavelengths, suggesting that stepwise *N*-de-methylation and destruction of the chromophore structure pathways would be occurring. However, the dramatically depletion of the absorbance with a slight blue shift during 0-180 min of irradiation imply that the destruction of the chromophore structure predominates over *N*-demethylation [49]. After being irradiated for 240 and 300 min, the characteristic band of MB significantly shifts to the shorter wavelengths, indicating that the *N*-de-methylation of MB molecules becomes a considerable pathway. The broad absorption bands in the visible range of 608-655 nm originates from the mixtures of Azure A, Azure B and Azure C intermediates that are derived from the *N*-de-methylation of MB [50,51]. Total organic carbon (TOC) analysis was further performed in order to determine the mineralization of MB during the photodegradation process. **Fig. S7(b)** shows that 33.4% and 3.2% of TOC are removed after 300 min of the MB photodegradation reaction using 12.5%wt-$Bi_2WO_6/ZnIn_2S_4$ and $ZnIn_2S_4$ as photocatalysts, respectively. This result implies that the original MB molecules are partly degraded into CO_2, water and/or inorganic species and almost transformed to *N*-de-methylated intermediates as mentioned above. Although the 12.5%wt-$Bi_2WO_6/ZnIn_2S_4$ photocatalyst cannot achieve complete mineralization, this photocatalyst has a relatively enhanced photocatalytic degradation activity and mineralization ability for MB in comparison to the $ZnIn_2S_4$ photocatalyst.

Active species trapping experiments on the photodegradation of SA are presented in **Fig. 8(f)**. The additions of ASC and EDTA-2Na significantly suppress the photodegradation rate. Meanwhile, employing iPrOH or $K_2S_2O_8$ also reduces the degradation efficiency, suggesting that $O_2^{\bullet-}$ and $^{\bullet}OH$ radicals as well as h^+ and e^- are responsible for the degradation reactions. The generation of $O_2^{\bullet-}$ can be proved by using the well-known nitrotetrazolium blue

transformation (NBT) method, respectively [33]. The $O_2^{\bullet-}$ radicals that are generated by O_2 reduction during the photocatalytic reaction can react with NBT to form the soluble blue formazan in aqueous solution, which shows an UV-vis absorption spectrum at absorption maximum of 265 nm. The decrease in absorbance at an absorption maximum indicates the higher NBT conversion which correlates to the increase in the generated $O_2^{\bullet-}$ radical. The absorption spectra of the NBT supernatant solutions after the $O_2^{\bullet-}$ detection test are shown in **Fig. S8(a)**. The 12.5%wt-Bi_2WO_6/$ZnIn_2S_4$ photocatalyst exhibits lower intensity of absorption peak when compared to $ZnIn_2S_4$. In a similar way, the $^{\bullet}$OH radicals can be detected by the benzoic acid hydroxylation, followed by the complexation with Fe(III) ion [34]. The generated $^{\bullet}$OH radicals can react with benzoic acid to yield *o*-hydroxybenzoic acid, and the *o*-hydroxybenzoic acid can form complex with Fe^{3+} ion added. Thereby, the $^{\bullet}$OH radicals generated during the photocatalytic reaction can be investigated by measuring the absorbance of the Fe(III)-hydroxybenzoic acid complex in the supernatant solution at a wavelength of 520 nm. The increase in the absorption intensity signifies the higher concentration of Fe(III)-hydroxybenzoic acid complex, relating to the increase in the generated $^{\bullet}$OH radical. The absorption spectra of the complex solutions after the $^{\bullet}$OH detection test are shown in **Fig. S8(b)**. The 12.5%wt-Bi_2WO_6/$ZnIn_2S_4$ photocatalyst presents the higher intensity of absorption peak when compared to $ZnIn_2S_4$. These results confirm that the $O_2^{\bullet-}$ and $^{\bullet}$OH radicals are photo-generated during the photocatalytic reactions.

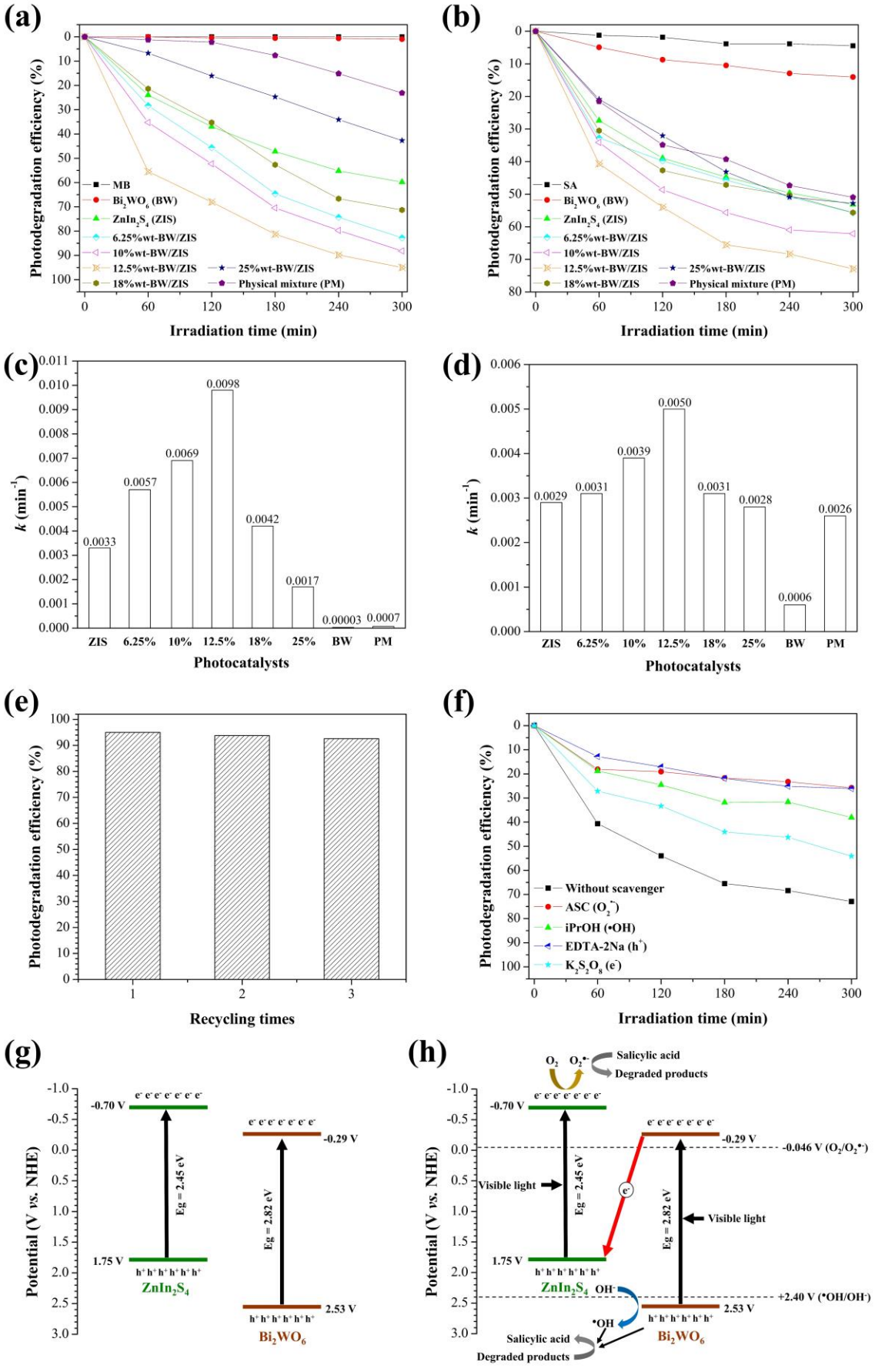
(a)
Photodegradation efficiency (%)
Irradiation time (min)
MB
Bi2WO6 (BW)
ZnIn2S4 (ZIS)
6.25%wt-BW/ZIS
10%wt-BW/ZIS
12.5%wt-BW/ZIS
18%wt-BW/ZIS
25%wt-BW/ZIS
Physical mixture (PM)
(b)
Photodegradation efficiency (%)
Irradiation time (min)
SA
Bi2WO6 (BW)
ZnIn2S4 (ZIS)
6.25%wt-BW/ZIS
10%wt-BW/ZIS
12.5%wt-BW/ZIS
18%wt-BW/ZIS
25%wt-BW/ZIS
Physical mixture (PM)
(c)
k (min-1)
0.0033
0.0057
0.0069
0.0098
0.0042
0.0017
0.00003
0.0007
ZIS
6.25%
10%
12.5%
18%
25%
BW
PM
Photocatalysts
(d)
k (min-1)
0.0029
0.0031
0.0039
0.0050
0.0031
0.0028
0.0006
0.0026
ZIS
6.25%
10%
12.5%
18%
25%
BW
PM
Photocatalysts
(e)
Photodegradation efficiency (%)
Recycling times
(f)
Photodegradation efficiency (%)
Irradiation time (min)
Without scavenger
ASC (O2•-)
iPrOH (•OH)
EDTA-2Na (h+)
K2S2O8 (e-)
(g)
Potential (V vs. NHE)
-0.70 V
1.75 V
Eg = 2.45 eV
ZnIn2S4
-0.29 V
2.53 V
Eg = 2.82 eV
Bi2WO6
(h)
O2
O2•-
Salicylic acid
Degraded products
-0.70 V
1.75 V
Eg = 2.45 eV
ZnIn2S4
Visible light
-0.29 V
-0.046 V (O2/O2•-)
Eg = 2.82 eV
Visible light
OH-
+2.40 V (•OH/OH-)
2.53 V
Bi2WO6
•OH
Salicylic acid
Degraded products

Fig. 8. Photodegradation efficiency of all photocatalysts towards **(a)** MB and **(b)** SA. The rate constants of the photodegradation of **(c)** MB and **(d)** SA. **(e)** Recyclability of 12.5%wt-$Bi_2WO_6/ZnIn_2S_4$ for the photodegradation of MB. **(f)** Effect of scavengers on the photodegradation efficiency of SA. **(g)** A proposed staggered band alignment. **(h)** Charge transfer mechanism for the photodegradation of SA over 12.5%wt-$Bi_2WO_6/ZnIn_2S_4$.

Based on the data obtained from the Mott-Schottky plots and UV-vis DRS analysis, the staggered band alignment for the $Bi_2WO_6/ZnIn_2S_4$ heterojunction are illustrated in **Fig. 8(g)**. With this alignment, two plausible charge transfer mechanisms – "conventional" and "Z-scheme" mechanisms – could be suggested [18,24]. Under visible light radiation, both Bi_2WO_6 and $ZnIn_2S_4$ in the $Bi_2WO_6/ZnIn_2S_4$ heterojunction produce holes (h^+) and electrons (e^-) at their VB and CB, respectively. After that, electrons at CB of $ZnIn_2S_4$ could move to CB of Bi_2WO_6 and holes at VB of Bi_2WO_6 could move to VB of $ZnIn_2S_4$ as illustrated in **Fig. S9**. According to this charge transfer pathway, due to the E_{CB} of Bi_2WO_6 (-0.29 V) is more negative than the reduction potential of $O_2/O_2^{\bullet-}$ (-0.046 V *vs.* NHE) [1], the electrons accumulated at its CB can reduce O_2 into $O_2^{\bullet-}$ radicals. However, holes at VB of $ZnIn_2S_4$ cannot oxidize OH^- to form $^{\bullet}OH$ radicals because of the less positive E_{VB} of $ZnIn_2S_4$ (1.75 V) than the reduction potential of $^{\bullet}OH/OH^-$ (+2.40 V *vs.* NHE) [24]. These findings are inconsistent with the results revealed from the trapping experiments (**Fig. 8(f)**). Therefore, charge transfer pathway in the $Bi_2WO_6/ZnIn_2S_4$ heterojunction would occur through the Z-scheme mechanism (**Fig. 8(h)**) rather than the conventional mechanism (**Fig. S9**). The Z-scheme mechanism can be briefly described as follows: after the heterojunction photocatalyst being exposed to the light, $ZnIn_2S_4$ and Bi_2WO_6 generate e^-/h^+ pairs. The electrons, accumulated at CB of Bi_2WO_6 (E_{CB} = -0.29 V), move to the more positive VB of $ZnIn_2S_4$ (E_{VB} = 1.75 V). As a result, the e^-/h^+ pairs are

separated and thus their recombination process is hindered as mentioned in the PL and EIS results (**Fig. 7(c)-(d)**). The $O_2^{\bullet-}$ radicals can be generated at CB of $ZnIn_2S_4$ which then directly degrade the molecule of SA. At the same time, holes that have high reduction potential, accumulated at VB of Bi_2WO_6 (E_{VB} = 2.53 V), can preferentially react with SA. In addition, holes can also oxidize OH^- to produce $^{\bullet}OH$ radicals.

3.2.3. Photocatalytic H_2 production

The $Bi_2WO_6/ZnIn_2S_4$ photocatalysts were also applied for the photocatalytic reduction of water, where methanol was used as a sacrificial reagent. The $Bi_2WO_6/ZnIn_2S_4$ with 6.25, 12.5 and 25%wt of Bi_2WO_6 can produce 297.5, 395.5 and 175.1 $\mu molg^{-1}$ of H_2 gas within 180 min (**Fig. 9(a)**). The highest amount of H_2 production is achieved on the 12.5%wt-$Bi_2WO_6/ZnIn_2S_4$ heterojunction photocatalyst (395.5 $\mu molg^{-1}$) which is about 1.5 times higher than that of $ZnIn_2S_4$ (267.5 $\mu molg^{-1}$). For Bi_2WO_6, H_2 gas cannot be produced. This is likely due to the rapid e^-/h^+ recombination rate of Bi_2WO_6 as well as the poor e^-/h^+ migration to its surface as referred in the PL and EIS results. The photocatalytic H_2 production rate of the $Bi_2WO_6/ZnIn_2S_4$ photocatalyst compared with the previous literatures that relates to $ZnIn_2S_4$-based heterojunction photocatalysts including other heterojunction photocatalysts are shown in **Table 1**. The variation in the H_2 production rates could be caused by the differences in the photocatalytic conditions used such as the light source power and type/concentration of sacrificial reagents. The recyclability of the 12.5%wt-$Bi_2WO_6/ZnIn_2S_4$ photocatalyst was investigated in three consecutive runs of H_2 production reaction. As shown in **Fig. 9(b),** the photocatalytic production activity shows no significant loss after three runs. Additionally, XRD patterns (**Fig. 9(c)**) of the photocatalyst samples before and after the recyclability test show negligible changes in the diffraction intensity as well as the diffraction position of both $ZnIn_2S_4$ and Bi_2WO_6 parts. Moreover, as illustrated in the FESEM image (**Fig. 9(d)**), the morphology

of this heterojunction photocatalyst is retained after the recyclability test. These results indicate reusability and excellent stability of the $Bi_2WO_6/ZnIn_2S_4$ heterojunction which are vital for practical application.

Table 1. Comparison of the photocatalytic H_2 production rate of the $Bi_2WO_6/ZnIn_2S_4$ photocatalyst with the previous literatures related to $ZnIn_2S_4$-based heterojunction photocatalysts including other heterojunction photocatalysts.

Photocatalyst	**Weight (mg)**	**Light source details**	**Sacrificial reagent**	**H_2 production rate ($\mu mol\ h^{-1}\ g^{-1}$)**
$Bi_2WO_6/ZnIn_2S_4$ (Our work)	20	150 W Xe	Methanol	131.8
$ZnIn_2S_4/In_2S_3$ [52]	100	300 W Xe	Na_2S/K_2SO_3	67.8
$MoS_2/ZnIn_2S_4$ [53]	50	300 W Xe	Na_2S/Na_2SO_3	120
$MoS_2/ZnIn_2S_4$ [29]	100	150 W Xe	Na_2S/Na_2SO_3	200.1
$WS_2/ZnIn_2S_4$ [54]	100	150 W Xe	Na_2S/Na_2SO_3	293.3
$ZnIn_2S_4/g\text{-}C_3N_4$ [55]	5	300 W Xe	Triethanolamine	282
MoS_2/Bi_2O_3 [56]	25	300 W Xe	Triethanolamine	615.0
$g\text{-}C_3N_4/NaTi_3O_7/V_2O_5$ [57]	50	300 W Xe	Na_2S/Na_2SO_3	567.2
$g\text{-}C_3N_4$/Co-MOF (ZIF-67) [58]	5	300 W Xe	Lactic acid	302.7
$g\text{-}C_3N_4/Nb_2O_5$ [59]	25	150 W white LED	Lactic acid	753
WS_2/ZrO_2 [60]	N/A	300 W Xe	Methanol	1023.9

The knowledge of E_{CB} and E_{VB} of semiconductors with respect to the reduction potentials of H^+/H_2 (0 V *vs*. NHE) and O_2/H_2O (+1.23 V *vs*. NHE) is essential to meet the success in the H_2 production. **Fig. 9(g)** illustrates that the E_{CB} and E_{VB} of $ZnIn_2S_4$ and Bi_2WO_6 in the $Bi_2WO_6/ZnIn_2S_4$ heterojunction are suitable for photocatalytic water splitting. The

photocatalytic process begins when the heterojunction photocatalyst is exposed to visible light. Both $ZnIn_2S_4$ and Bi_2WO_6 in the $Bi_2WO_6/ZnIn_2S_4$ heterojunction are activated, and thus e^-/h^+ pairs are generated. Simultaneously, electrons at CB of Bi_2WO_6 recombine with holes at VB of $ZnIn_2S_4$, following the direct Z-scheme mechanism. In this mechanism, H^+ is reduced by the highly reductive electrons at CB of $ZnIn_2S_4$, in the meantime, the strong oxidative holes at VB of Bi_2WO_6 are consumed by methanol to form oxidation products (**Fig. 9(e)**). The step-wise mechanisms are proposed as follows:

$$Bi_2WO_6/ZnIn_2S_4 + \text{visible light} \rightarrow Bi_2WO_6\ (e^- \text{ and } h^+) + ZnIn_2S_4\ (e^- \text{ and } h^+) \quad (4)$$

$$Bi_2WO_6\ (e^- \text{ and } h^+) + ZnIn_2S_4\ (e^- \text{ and } h^+) \rightarrow Bi_2WO_6\ (h_{VB}^+) + ZnIn_2S_4\ (e_{CB}^-) \quad (5)$$

$$2H^+ + 2e^- \text{ at CB of } ZnIn_2S_4 \rightarrow H_2 \quad (6)$$

$$\text{methanol} + h^+ \text{ at VB of } Bi_2WO_6 \rightarrow \text{oxidation products} \quad (7)$$

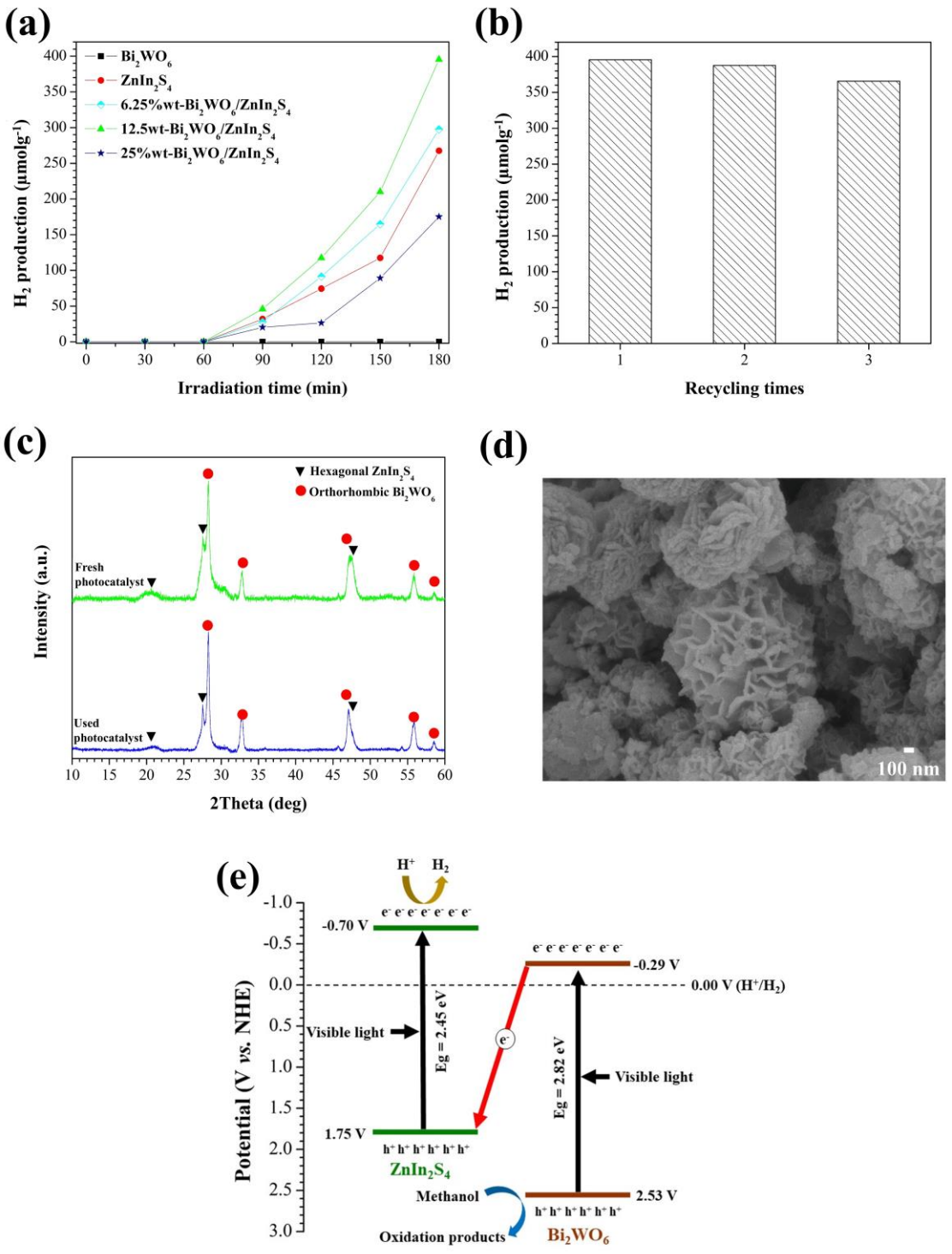

Fig. 9. (a) Photocatalytic H_2 production of $Bi_2WO_6/ZnIn_2S_4$ with different amount of Bi_2WO_6 in comparison with the Bi_2WO_6 and $ZnIn_2S_4$ photocatalysts. **(b)** Cyclic H_2 production on 12.5%wt-$Bi_2WO_6/ZnIn_2S_4$. **(c)** XRD spectra of fresh and used 12.5%wt-$Bi_2WO_6/ZnIn_2S_4$ photocatalyst and **(d)** FESEM image of the used 12.5%wt-$Bi_2WO_6/ZnIn_2S_4$ photocatalyst. **(e)** Charge transfer mechanism for H_2 production by $Bi_2WO_6/ZnIn_2S_4$ heterojunction.

4. Conclusions

The direct Z-scheme $Bi_2WO_6/ZnIn_2S_4$ heterojunction, synthesized in this work, significantly enhanced the photodegradation of MB and SA, and also enhanced the production of H_2 gas with high stability and renewable performance. The photo-efficacy of the heterojunction was maximized after adding a small amount of Bi_2WO_6 (12.5%wt). The morphological characterizations of this photocatalyst revealed that the spherical Bi_2WO_6 nanoparticles were finely distributed on the $ZnIn_2S_4$ nanosheets, forming the $Bi_2WO_6/ZnIn_2S_4$ heterojunction structure. The optical characterizations and electrochemical measurements of this heterojunction indicated that the UV-vis DRS spectrum shifted towards longer wavelength region in comparison to that of Bi_2WO_6, and this heterojunction provided the reduction in probability of charge recombination and the enhancement of charge transportation. The enhancement in the photocatalytic activity is derived from the effective utilization of light and the Z-scheme band structure of $Bi_2WO_6/ZnIn_2S_4$ with intimate contact. This heterojunction displays good ability for the applications in wastewater purification and production of renewable energy.

Acknowledgements

This research work was partially supported by Chiang Mai University. Financial support from the Program Management Unit – Brain Power (PMU B); the Office of National Higher Education Science Research and Innovation Policy Council (NXPO) in Global Partnership Project; the Center of Excellence for Innovation in Chemistry (PERCH-CIC), Ministry of Higher Education, Science, Research and Innovation; and the Institute for the Promotion of Teaching Science and Technology (IPST) are acknowledged.

Conflicts of Interest: The authors declare that there are no conflicts of interest.

References

[1] H. Xu, Y. Jiang, X. Yang, F. Li, A. Li, Y. Liu, J. Zhang, Z. Zhou, L. Ni, Fabricating carbon quantum dots doped $ZnIn_2S_4$ nanoflower composites with broad spectrum and enhanced photocatalytic Tetracycline hydrochloride degradation, Mater. Res. Bull. 97 (2018) 158–168. doi:10.1016/j.materresbull.2017.09.004.

[2] A.A. Ismail, D.W. Bahnemann, Photochemical splitting of water for hydrogen production by photocatalysis: A review, Sol. Energy Mater. Sol. Cells. 128 (2014) 85–101. doi:10.1016/j.solmat.2014.04.037.

[3] M. Zhang, Y. Zhu, W. Li, F. Wang, H. Li, X. Liu, W. Zhang, C. Ren, Double Z-scheme system of silver bromide@bismuth tungstate/tungsten trioxide ternary heterojunction with enhanced visible-light photocatalytic activity, J. Colloid Interface Sci. 509 (2018) 18–24. doi:10.1016/j.jcis.2017.08.095.

[4] Z. Xiao, J. Zhang, Y. Xia, L. Zhu, L. Lei, S. Xu, Nanoplates-assembled Bi_2WO_6 microcoins with hierarchical porous structure as efficient visible-light-active photocatalysts, Mater. Res. Bull. 94 (2017) 322–327. doi:10.1016/j.materresbull.2017.06.013.

[5] F. Wang, W. Li, S. Gu, H. Li, X. Wu, C. Ren, X. Liu, Facile fabrication of direct Z-scheme MoS_2/Bi_2WO_6 heterojunction photocatalyst with superior photocatalytic performance under visible light irradiation, J. Photochem. Photobiol. A Chem. 335 (2017) 140–148. doi:10.1016/j.jphotochem.2016.11.026.

[6] Z. Chen, J. Xu, Z. Ren, Y. He, G. Xiao, Low temperature synthesis of $ZnIn_2S_4$ microspheres as a visible light photocatalyst for selective oxidation, Catal. Commun. 41 (2013) 83–86. doi:10.1016/j.catcom.2013.07.016.

[7] K. Zhang, L. Guo, Metal sulphide semiconductors for photocatalytic hydrogen production, Catal. Sci. Technol. 3 (2013) 1672. doi:10.1039/c3cy00018d.

[8] A. Hernández-Ramírez, I. Medina-Ramírez, Photocatalytic Semiconductors, Springer, Switzerland, 2015. doi:10.1007/978-3-319-10999-2.

[9] N.S. Chaudhari, A.P. Bhirud, R.S. Sonawane, L.K. Nikam, S.S. Warule, V.H. Rane, B.B. Kale, Ecofriendly hydrogen production from abundant hydrogen sulfide using solar light-driven hierarchical nanostructured $ZnIn_2S_4$ photocatalyst, Green Chem. 13 (2011) 2500. doi:10.1039/c1gc15515f.

[10] L. Su, X. Ye, S. Meng, X. Fu, S. Chen, Effect of different solvent on the photocatalytic activity of $ZnIn_2S_4$ for selective oxidation of aromatic alcohols to aromatic aldehydes under visible light irradiation, Appl. Surf. Sci. 384 (2016) 161–174. doi:10.1016/j.apsusc.2016.04.084.

[11] S. Adhikari, A.V.K. Charanpahari, G. Madras, Solar-light-driven improved photocatalytic performance of hierarchical $ZnIn_2S_4$ architectures, ACS Omega. 2 (2017) 6926–6938. doi:10.1021/acsomega.7b01329.

[12] S. Peng, L. Li, Y. Wu, L. Jia, L. Tian, M. Srinivasan, S. Ramakrishna, Q. Yan, S.G. Mhaisalkar, Size- and shape-controlled synthesis of $ZnIn_2S_4$ nanocrystals with high photocatalytic performance, CrystEngComm. 15 (2013) 1922–1930. doi:10.1039/c2ce26593a.

[13] S. Shen, L. Zhao, Z. Zhou, L. Guo, Enhanced photocatalytic hydrogen evolution over Cu-doped $ZnIn_2S_4$ under visible light, J. Phys. Chem. C. 112 (2008) 16148. doi:10.1021/jp804525q.

[14] Q. Liu, H. Lu, Z. Shi, F. Wu, J. Guo, K. Deng, L. Li, 2D $ZnIn_2S_4$ nanosheet/1D TiO_2 nanorod heterostructure arrays for improved photoelectrochemical water splitting, Appl. Mater. Interfaces. 6 (2014) 17200–17207. doi:10.1021/am505015j.

[15] W. Shi, H. Lv, S. Yuan, H. Huang, Y. Liu, Z. Kang, Synergetic effect of carbon dots as co-catalyst for enhanced photocatalytic performance of methyl orange on $ZnIn_2S_4$ microspheres, Sep. Purif. Technol. 174 (2017) 282–289. doi:10.1016/j.seppur.2016.11.013.

[16] S. Xu, J. Dai, J. Yang, J. You, J. Hao, Facile synthesis of novel $CaIn_2S_4/ZnIn_2S_4$ composites with efficient performance for photocatalytic reduction of Cr(VI) under simulated sunlight irradiation, Nanomaterials. 8 (2018). doi:10.3390/nano8070472.

[17] R. Marschall, Semiconductor composites: Strategies for enhancing charge carrier separation to improve photocatalytic activity, Adv. Funct. Mater. 24 (2014) 2421–2440. doi:10.1002/adfm.201303214.

[18] A. Chachvalvutikul, W. Pudkon, T. Luangwanta, T. Thongtem, S. Thongtem, S. Kittiwachana, S. Kaowphong, Enhanced photocatalytic degradation of methylene blue by a direct Z-scheme $Bi_2S_3/ZnIn_2S_4$ photocatalyst, Mater. Res. Bull. 111 (2019) 53–60. doi:10.1016/j.materresbull.2018.10.034.

[19] R. Jiang, D. Wu, G. Lu, Z. Yan, J. Liu, Modified 2D-2D $ZnIn_2S_4$/BiOCl van der Waals heterojunctions with CQDs: Accelerated charge transfer and enhanced photocatalytic activity under vis- and NIR-light, Chemosphere. 227 (2019) 82–92. doi:10.1016/j.chemosphere.2019.04.038.

[20] D. Yuan, M. Sun, S. Tang, Y. Zhang, Z. Wang, J. Qi, Y. Rao, Q. Zhang, All-solid-state $BiVO_4/ZnIn_2S_4$ Z-scheme composite with efficient charge separations for improved visible light photocatalytic organics degradation, Chinese Chem. Lett. 31 (2020) 547–550. doi:10.1016/j.cclet.2019.09.051.

[21] S. Wan, Q. Zhong, M. Ou, S. Zhang, Synthesis and characterization of direct Z-scheme $Bi_2MoO_6/ZnIn_2S_4$ composite photocatalyst with enhanced photocatalytic oxidation of NO under visible light, J. Mater. Sci. 52 (2017) 11453–11466. doi:10.1007/s10853-017-

1283-3.

[22] F. Qin, P. Cui, L. Hu, Z. Wang, J. Chen, X. Xing, H. Wang, Construction of multi-shelled Bi_2WO_6 hollow microspheres with enhanced visible light photo-catalytic performance, Mater. Res. Bull. 99 (2018) 331–335. doi:10.1016/j.materresbull.2017.11.016.

[23] A. Kaur, S.K. Kansal, Bi_2WO_6 nanocuboids: An efficient visible light active photocatalyst for the degradation of levofloxacin drug in aqueous phase, Chem. Eng. J. 302 (2016) 194–203. doi:10.1016/j.cej.2016.05.010.

[24] W.-K. Jo, J.Y. Lee, T.S. Natarajan, Fabrication of hierarchically structured novel redox-mediator-free $ZnIn_2S_4$ marigold flower/Bi_2WO_6 flower-like direct Z-scheme nanocomposite photocatalysts with superior visible light photocatalytic efficiency., Phys. Chem. Chem. Phys. 18 (2016) 1000–16. doi:10.1039/c5cp06176h.

[25] A.M. Yang, Y. Han, S.S. Li, H.W. Xing, Y.H. Pan, W.X. Liu, Synthesis and comparison of photocatalytic properties for Bi_2WO_6 nanofibers and hierarchical microspheres, J. Alloys Compd. 695 (2017) 915–921. doi:10.1016/j.jallcom.2016.10.188.

[26] V. Shivani, S. Harish, J. Archana, M. Navaneethan, S. Ponnusamy, Y. Hayakawa, Highly efficient 3-D hierarchical Bi_2WO_6 catalyst for environmental remediation, Appl. Surf. Sci. 488 (2019) 696–706. doi:10.1016/j.apsusc.2019.05.072.

[27] Y.-J. Zhu, F. Chen, Microwave-assisted preparation of inorganic nanostructures in liquid phase, Chem. Rev. 114 (2013) 6462–6555. doi:10.1021/cr400366s.

[28] T. Thongtem, S. Kaowphong, S. Thongtem, Influence of cetyltrimethylammonium bromide on the morphology of AWO_4 (A = Ca, Sr) prepared by cyclic microwave irradiation, Appl. Surf. Sci. 254 (2008). doi:10.1016/j.apsusc.2008.02.024.

[29] W. Pudkon, H. Bahruji, P.J. Miedziak, T.E. Davies, D.J. Morgan, S. Pattisson, S.K.G.J. Hutchings, Enhanced visible-light-driven photocatalytic H_2 production and Cr(VI)

reduction of a $ZnIn_2S_4/MoS_2$ heterojunction synthesized by the biomolecule-assisted microwave heating method, Catal. Sci. Technol. (2020). doi:10.1039/D0CY00234H.

[30] J. Lv, Q. Hu, C. Cao, Y. Zhao, Modulation of valence band maximum edge and photocatalytic activity of BiOX by incorporation of halides, Chemosphere. 191 (2018) 427–437. doi:10.1016/j.chemosphere.2017.09.149.

[31] H. Fu, C. Pan, W. Yao, Y. Zhu, Visible-light-induced degradation of rhodamine B by nanosized Bi_2WO_6, J. Phys. Chem. B. 109 (2005) 22432–22439. doi:10.1021/jp052995j.

[32] J. Yu, S. Zhuang, X. Xu, W. Zhu, B. Feng, J. Hu, Photogenerated electron reservoir in hetero-p-n CuO-ZnO nanocomposite device for visible-light-driven photocatalytic reduction of aqueous Cr(vi), J. Mater. Chem. A. 3 (2015) 1199–1207. doi:10.1039/c4ta04526b.

[33] L. Acharya, S. Nayak, S.P. Pattnaik, R. Acharya, K. Parida, Resurrection of boron nitride in p-n type-II boron nitride/B-doped-g-C_3N_4 nanocomposite during solid-state Z-scheme charge transfer path for the degradation of tetracycline hydrochloride, J. Colloid Interface Sci. 566 (2020) 211–223. doi:10.1016/j.jcis.2020.01.074.

[34] S. Gazi, R. Ananthakrishnan, Semi-quantitative determination of hydroxyl radicals by benzoic acid hydroxylation: An analytical methodology for photo-fenton systems, Curr. Anal. Chem. 8 (2011) 143–149. doi:10.2174/157341112798472297.

[35] S. Shen, L. Zhao, L. Guo, Morphology, structure and photocatalytic performance of $ZnIn_2S_4$ synthesized via a solvothermal/hydrothermal route in different solvents, J. Phys. Chem. Solids. 69 (2008) 2426–2432. doi:10.1016/j.jpcs.2008.04.035.

[36] H. Wang, Y. Xia, H. Li, X. Wang, Y. Yu, X. Jiao, D. Chen, Highly active deficient ternary sulfide photoanode for photoelectrochemical water splitting, Nat. Commun. 11 (2020) 1–11. doi:10.1038/s41467-020-16800-w.

[37] Y. Wang, D. Chen, L. Qin, J. Liang, Y. Huang, Hydrogenated $ZnIn_2S_4$ microspheres:

Boosting photocatalytic hydrogen evolution by sulfur vacancy engineering and mechanism insight, Phys. Chem. Chem. Phys. 21 (2019) 25484–25494. doi:10.1039/c9cp04709c.

[38] Z. Fang, S. Weng, X. Ye, W. Feng, Z. Zheng, M. Lu, S. Lin, X. Fu, P. Liu, Defect engineering and phase junction architecture of wide-bandgap ZnS for conflicting visible Light activity in photocatalytic H_2 evolution, ACS Appl. Mater. Interfaces. 7 (2015) 13915–13924. doi:10.1021/acsami.5b02641.

[39] J. Wedekind, L. Xu, S. V. Buldyrev, H.E. Stanley, D. Reguera, G. Franzese, Optimization of crystal nucleation close to a metastable fluid-fluid phase transition, Sci. Rep. 5 (2015) 1–7. doi:10.1038/srep11260.

[40] K.S.W. Sing, R.T. Williams, Physisorption hysteresis loops and the characterization of nanoporous materials, Adsorpt. Sci. Technol. 22 (2004) 773–782. doi:10.1260/0263617053499032.

[41] C. Liu, B. Chai, C. Wang, J. Yan, Z. Ren, Solvothermal fabrication of MoS_2 anchored on $ZnIn_2S_4$ microspheres with boosted photocatalytic hydrogen evolution activity, Int. J. Hydrogen Energy. (2018) 6977–6986. doi:10.1016/j.ijhydene.2018.02.116.

[42] A. Chachvalvutikul, J. Jakmunee, S. Thongtem, S. Kittiwachana, S. Kaowphong, Novel $FeVO_4/Bi_7O_9I_3$ nanocomposite with enhanced photocatalytic dye degradation and photoelectrochemical properties, Appl. Surf. Sci. 475 (2019) 175–184. doi:10.1016/j.apsusc.2018.12.214.

[43] B. Chai, C. Liu, C. Wang, J. Yan, Z. Ren, Photocatalytic hydrogen evolution activity over $MoS_2/ZnIn_2S_4$ microspheres, Chinese J. Catal. 38 (2017) 2067–2075. doi:10.1016/S1872-2067(17)62981-4.

[44] X. Chen, Y. Li, L. Li, Facet-engineered surface and interface design of WO_3/Bi_2WO_6 photocatalyst with direct Z-scheme heterojunction for efficient salicylic acid removal,

Appl. Surf. Sci. 508 (2020) 144796. doi:10.1016/j.apsusc.2019.144796.

[45] C. Feng, L. Tang, Y. Deng, J. Wang, Y. Liu, X. Ouyang, Z. Chen, H. Yang, J. Yu, J. Wang, Maintaining stable LSPR performance of $W_{18}O_{49}$ by protecting its oxygen vacancy: A novel strategy for achieving durable sunlight driven photocatalysis, Appl. Catal. B Environ. 276 (2020) 119167. doi:10.1016/j.apcatb.2020.119167.

[46] L. Tang, C. Feng, Y. Deng, G. Zeng, J. Wang, Y. Liu, H. Feng, J. Wang, Enhanced photocatalytic activity of ternary Ag/g-C_3N_4/$NaTaO_3$ photocatalysts under wide spectrum light radiation: The high potential band protection mechanism, Appl. Catal. B Environ. 230 (2018) 102–114. doi:10.1016/j.apcatb.2018.02.031.

[47] C. Feng, L. Tang, Y. Deng, J. Wang, W. Tang, Y. Liu, Z. Chen, J. Yu, J. Wang, Q. Liang, Synthesis of branched WO_3@$W_{18}O_{49}$ homojunction with enhanced interfacial charge separation and full-spectrum photocatalytic performance, Chem. Eng. J. 389 (2020) 124474. doi:10.1016/j.cej.2020.124474.

[48] W. Gan, J. Zhang, H. Niu, L. Bao, H. Hao, Y. Yan, K. Wu, X. Fu, Fabrication of Ag/AgBr/Bi_2WO_6 hierarchical composites with high visible light photocatalytic activity, Chem. Phys. Lett. 737 (2019) 136830. doi:10.1016/j.cplett.2019.136830.

[49] K. Yu, S. Yang, H. He, C. Sun, C. Gu, Y. Ju, Visible light-driven photocatalytic degradation of rhodamine B over $NaBiO_3$: Pathways and mechanism, J. Phys. Chem. A. 113 (2009) 10024–10032. doi:10.1021/jp905173e.

[50] J. Luan, Z. Hu, Synthesis, property characterization, and photocatalytic activity of novel visible light-responsive photocatalyst Fe_2BiSbO_7, Int. J. Photoenergy. 2012 (2012). doi:10.1155/2012/301954.

[51] T. Zhang, T. Oyama, A. Aoshima, H. Hidaka, J. Zhao, N. Serpone, Photooxidative N-demethylation of methylene blue in aqueous TiO_2 dispersions under UV irradiation, J. Photochem. Photobiol. A Chem. 140 (2001) 163–172. doi:10.1016/S1010-

6030(01)00398-7.

[52] Z. Mei, S. Ouyang, D.-M. Tang, T. Kako, D. Golberg, J. Ye, An ion-exchange route for the synthesis of hierarchical $In_2S_3/ZnIn_2S_4$ bulk composite and its photocatalytic activity under visible-light irradiation., Dalt. Trans. 42 (2013) 2687–90. doi:10.1039/c2dt32271d.

[53] T. Huang, W. Chen, T.Y. Liu, Q.L. Hao, X.H. Liu, $ZnIn_2S_4$ hybrid with MoS_2: A non-noble metal photocatalyst with efficient photocatalytic activity for hydrogen evolution, Powder Technol. 315 (2017) 157–162. doi:10.1016/j.powtec.2017.03.054.

[54] W. Pudkon, S. Kaowphong, S. Pattison, P.J. Miedziak, H. Bahruji, T.E. Davies, D.J. Morgan, G.I. Hutchings, Microwave synthesis of $ZnIn_2S_4/WS_2$ composites for photocatalytic hydrogen production and hexavalent chromium reduction, Catal. Sci. Technol. (2019). doi:10.1039/C9CY01553A.

[55] Z. Zhang, K. Liu, Z. Feng, Y. Bao, B. Dong, Hierarchical Sheet-on-Sheet $ZnIn_2S_4$/g-C_3N_4 Heterostructure with Highly Efficient Photocatalytic H_2 production Based on Photoinduced Interfacial Charge Transfer, Sci. Rep. 6 (2016) 19221. doi:10.1038/srep19221.

[56] B.S. Goud, G. Koyyada, J.H. Jung, G.R. Reddy, J. Shim, N.D. Nam, S.V.P. Vattikuti, Surface oxygen vacancy facilitated Z-scheme MoS_2/Bi_2O_3 heterojunction for enhanced visible-light driven photocatalysis-pollutant degradation and hydrogen production, Int. J. Hydrogen Energy. 45 (2020) 18961–18975. doi:10.1016/j.ijhydene.2020.05.073.

[57] S.V.P. Vattikuti, N.D. Nam, J. Shim, Graphitic carbon nitride/$Na_2Ti_3O_7/V_2O_5$ nanocomposite as a visible light active photocatalyst, Ceram. Int. 46 (2020) 18287–18296. doi:10.1016/j.ceramint.2020.05.045.

[58] K.C. Devarayapalli, S.V.P. Vattikuti, T.V.M. Sreekanth, K.S. Yoo, P.C. Nagajyothi, J. Shim, Hydrogen production and photocatalytic activity of g-C_3N_4/Co-MOF (ZIF-67)

nanocomposite under visible light irradiation, Appl. Organomet. Chem. 34 (2020) 1–9. doi:10.1002/aoc.5376.

[59] K.C. Devarayapalli, S.V. Prabhakar Vattikuti, T.V. Madhukar Sreekanth, P. Chidanandha Nagajyothi, J. Shim, Pyrolysis-synthesized g-C_3N_4/Nb_2O_5 nanocomposite for enhanced photocatalytic activity under white LED light irradiation, ChemistrySelect. 4 (2019) 13250–13258. doi:10.1002/slct.201902943.

[60] S.V.P. Vattikuti, K.C. Devarayapalli, P.C. Nagajyothi, J. Shim, Binder-free WS_2/ZrO_2 hybrid as a photocatalyst for organic pollutant degradation under UV/simulated sunlight and tests for H_2 evolution, J. Alloys Compd. 809 (2019) 151805. doi:10.1016/j.jallcom.2019.151805.